

Submitted by
Julian Hofer, B.Sc.

Submitted at
Institute of Semiconductor and Solid State Physics

Supervisor
Prof. Dr. Armando Rastelli

Co-Supervisor
DI Christian Schimpf

month year

Exciting and Resolving Quantum Dot Emission with Adiabatic Rapid Passage and Fabry Perot Interferometer



Master Thesis
to obtain the academic degree of
Diplom-Ingenieur
in the Master's Program
Technische Physik

Eidesstattliche Erklärung

Ich erkläre an Eides statt, dass ich die vorliegende Masterarbeit selbstständig und ohne fremde Hilfe verfasst, andere als die angegebenen Quellen und Hilfsmittel nicht benutzt bzw. die wörtlich oder sinngemäß entnommenen Stellen als solche kenntlich gemacht habe. Die vorliegende Masterarbeit ist mit dem elektronisch übermittelten Textdokument identisch.

Datum

Unterschrift

Acknowledgement

Hello, here is some text without a meaning. This text should show what a printed text will look like at this place. If you read this text, you will get no information. Really? Is there no information? Is there a difference between this text and some nonsense like "Huardest gefburn"? Kjift – not at all! A blind text like this gives you information about the selected font, how the letters are written and an impression of the look. This text should contain all letters of the alphabet and it should be written in of the original language. There is no need for special contents, but the length of words should match the language.

This document is set in Palatino, compiled with pdfL^AT_EX2e and Biber.

The L^AT_EX template from Karl Voit is based on KOMA script and can be found online:
<https://github.com/novoid/LaTeX-KOMA-template>

Abstract

This is a placeholder for the abstract. It summarizes the whole thesis to give a very short overview.
Usually, this the abstract is written when the whole thesis text is finished.

Contents

Abstract

1. Introduction	1
2. Droplet etched gallium arsenide quantum dots	3
2.1. Fabrication and optical properties	3
2.2. Fine structure splitting	6
2.3. Zero-phonon line and phonon sideband	7
2.4. Optical excitation of a quantum dot	10
2.5. Resonant two-photon excitation	10
2.6. Single photon emission	10
3. Single photon generation using adiabatic rapid passage with frequency-chirped pulses	11
3.1. Introduction and motivation	11
3.2. Fundamentals of chirp and interferometric autocorrelation	11
3.2.1. Chirp	11
3.2.2. Interferometric autocorrelation	11
3.2.3. Modified-spectrum autointerferometric correlation	11
3.3. Adiabatic rapid passage	11
3.4. Simulation	11
3.5. Measurements and discussion	11
4. Building up a scanning Fabry-Pérot interferometer from scratch	13
4.1. Introduction and motivation	13
4.2. Transverse modes of electromagnetic radiation	13
4.2.1. Gaussian beam	13
4.2.2. Higher Gauss modes	16

4.3.	Fundamentals of Fabry-Pérot interferometers	17
4.3.1.	Resonator losses	17
4.3.2.	Resonance frequencies, free spectral range and spectral line shapes	17
4.3.3.	Airy distribution of Fabry-Pérot interferometers	18
4.3.4.	Airy linewidth and finesse	20
4.3.5.	Mode matching and spatial filtering	22
4.3.6.	Confocal setup	24
4.4.	Simulation	25
4.5.	Setup	26
4.5.1.	Flat mirrors	26
4.5.2.	Concave mirrors	26
4.5.3.	Confocal setup	26
4.6.	Measurements and discussion	26
5.	Summary and conclusion	27
6.	Outlook	29
A.	Acronyms	33
Bibliography		35

List of Figures

2.1.	Droplet etched GaAs quantum dots.	4
2.2.	Biexciton-esciton cascade in a quantum dot (QD). [1]	5
2.3.	Height profile and AFM picture of a droplet-etched nanohole in an AlGaAs layer	5
2.4.	Fine structure splitting in a GaAs quantum dot.	6
2.5.	Absorption line shape of an electronic excitation.	7
2.6.	Zero-phonon line and phonon sideband. [9]	8
2.7.	Simulated exciton emission of a GaAs quantum dot	10
4.1.	A Gaussian beam near its beam waist.	14
4.2.	Gaussian modes higher order of a simple Ti-sapphire laser	16
4.3.	Fabry Pérot interferometer with electric field mirror reflectivities r_1 and r_2	19
4.4.	Airy distribution A'_{trans}	20
4.5.	Demonstration of the physical meaning of the Airy finesse F_{Airy}	21
4.6.	Incident monochromatic beam of light exciting transverse mode m, n of a resonator [15]	22
4.7.	Mode matching of an Gaussian beam into a Fabry Pérot interferometer.	23
4.8.	Spatial filtering of Gauss modes.	24
4.9.	Fabry Pérot interferometer	26

1. Introduction

Hello, here is some text without a meaning. This text should show what a printed text will look like at this place. If you read this text, you will get no information. Really? Is there no information? Is there a difference between this text and some nonsense like "Huardest gefburn"? Kjift – not at all! A blind text like this gives you information about the selected font, how the letters are written and an impression of the look. This text should contain all letters of the alphabet and it should be written in of the original language. There is no need for special contents, but the length of words should match the language.

This is the second paragraph. Hello, here is some text without a meaning. This text should show what a printed text will look like at this place. If you read this text, you will get no information. Really? Is there no information? Is there a difference between this text and some nonsense like "Huardest gefburn"? Kjift – not at all! A blind text like this gives you information about the selected font, how the letters are written and an impression of the look. This text should contain all letters of the alphabet and it should be written in of the original language. There is no need for special contents, but the length of words should match the language.

And after the second paragraph follows the third paragraph. Hello, here is some text without a meaning. This text should show what a printed text will look like at this place. If you read this text, you will get no information. Really? Is there no information? Is there a difference between this text and some nonsense like "Huardest gefburn"? Kjift – not at all! A blind text like this gives you information about the selected font, how the letters are written and an impression of the look. This text should contain all letters of the alphabet and it should be written in of the original language. There is no need for special contents, but the length of words should match the language.

After this fourth paragraph, we start a new paragraph sequence. Hello, here is some text without a meaning. This text should show what a printed text will look like at this place. If you read this text, you will get no information. Really? Is there no information? Is there a difference between this text and

1. Introduction

some nonsense like “Huardest gefburn”? Kjift – not at all! A blind text like this gives you information about the selected font, how the letters are written and an impression of the look. This text should contain all letters of the alphabet and it should be written in of the original language. There is no need for special contents, but the length of words should match the language.

Hello, here is some text without a meaning. This text should show what a printed text will look like at this place. If you read this text, you will get no information. Really? Is there no information? Is there a difference between this text and some nonsense like “Huardest gefburn”? Kjift – not at all! A blind text like this gives you information about the selected font, how the letters are written and an impression of the look. This text should contain all letters of the alphabet and it should be written in of the original language. There is no need for special contents, but the length of words should match the language.

2. Droplet etched gallium arsenide quantum dots

2.1. Fabrication and optical properties

Quantum dots (QD) are nanostructures which confine the motion of electrons and holes in all three-dimensional spatial dimensions. Confinement results in discrete energy levels, which is why QDs are sometimes referred to as *artificial atoms*. Additionally, they provide potentially suitable implementations of qbits, the basic unit of quantum information. The discussion in this section is based on the PhD thesis of Huber [1].

Gallium arsenide quantum dots investigated within this master's thesis are grown by molecular beam epitaxy (MBE) with the self-assembled nanodrill technology described in the work of Wang et al. [2]. As displayed in figure 2.1(a) the aluminium (Al) forms droplets on AlGaAs after evaporation. The Al reacts with AlGaAs, which leads into nanoholes etched into the surface. Under optimal conditions, these nanoholes are highly symmetric as can be seen in figure 2.1(b). This results into QD with high in-plane symmetry. The next step is the annealing process in which gallium arsenide (GaAs) is deposited to fill the nanoholes. The QD is finalized by capping the layer with AlGaAs acting as top barrier.

Compared to the band gap of the host material $\text{Al}_{0.4}\text{Ga}_{0.6}\text{As}$ of 1.92 eV at room temperature, the core of the QD, GaAs, has a band gap of only 1.42 eV at room temperature. This energy difference between the band gaps and nanosized dimensions of the QD are responsible for the 3D confinement and the type-I band alignment depicted in figure 2.1(c). This thesis focuses on optical transitions between the first energy level in the conduction band (CB) and the valence band (VB), often called the s-shell. The carriers are electrons e^- and the holes left behind h^+ . These are fermions and can therefore only up to two of them can, in accordance with Pauli's exclusion principle, occupy a single energy state. Electrons and holes are strongly localized inside the QD and interact with each other by Coulomb

2. Droplet etched gallium arsenide quantum dots

interaction. This leads to multi-particle complexes with the most fundamental being the exciton (X), a bound state of an electron and a hole. A fully occupied s-shell, can be described by the quasiparticle called biexciton (XX).

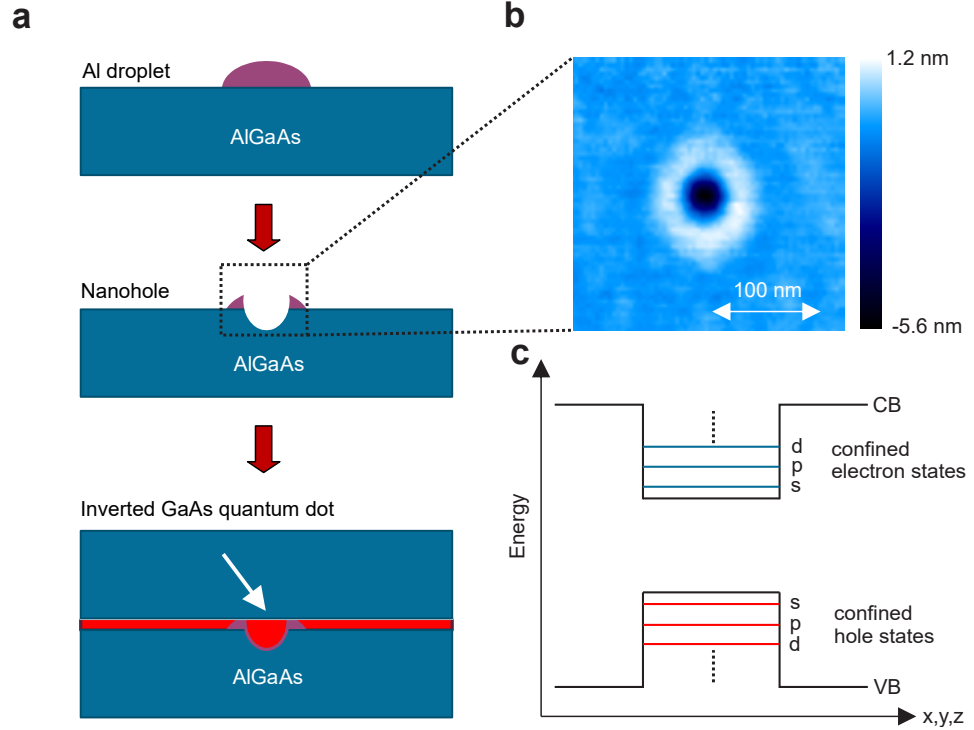


Figure 2.1.: (a) The growth process of a GaAs quantum dot by MBE.
 (b) Atomic force microscopy (AFM) image of the nanohole before it is filled with GaAs.
 (c) Conduction band (CB) and valence band (VB) of an optically active QD. [1]

In a QD polarization-entangled photon pairs can be generated via a biexciton-exciton cascade [3], illustrated in figure 2.2. $|XX\rangle$ forms a full shell, which means that the total angular momentum projection along the quantization axis of the XX complex sums up to $M = 0$. After exciting the QD into the $|XX\rangle$ state (e.g. by optical pumping) it decays by spontaneous recombination of an electron-hole-pair accompanied by the emission of a single photon into the $|X\rangle$ state. The two-dipole allowed radiative transitions lead to only two possible $|X\rangle$ states:

- $| -1 \rangle$ under emission of a right-circularly-polarized photon $|r\rangle$
- $| +1 \rangle$ under emission of a left-circularly-polarized photon $|l\rangle$

$| -1 \rangle$ and $| +1 \rangle$ are degenerate in energy and decay into the groundstate $|G\rangle$ under emission of $|l\rangle$ and $|r\rangle$, respectively.

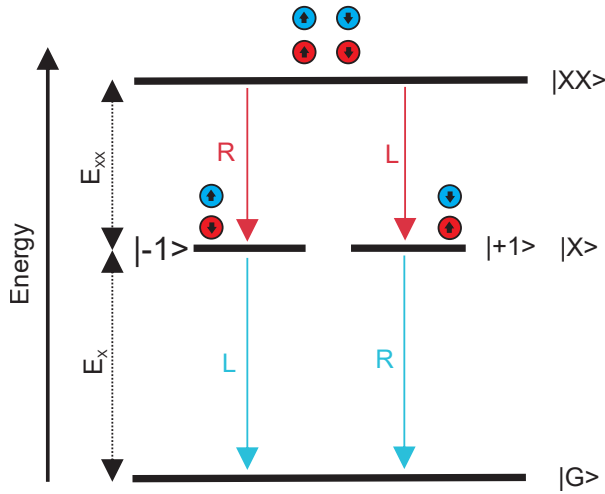


Figure 2.2.: Biexciton-esciton cascade in a QD. [1]

Figure 2.3 displays another perspective of GaAs QDs with a comparison of the order of magnitude of its height profile and wavefunction of the exciton.

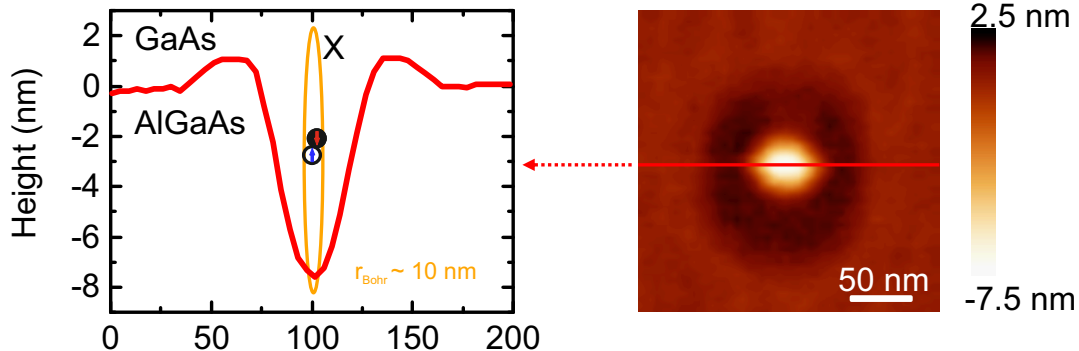
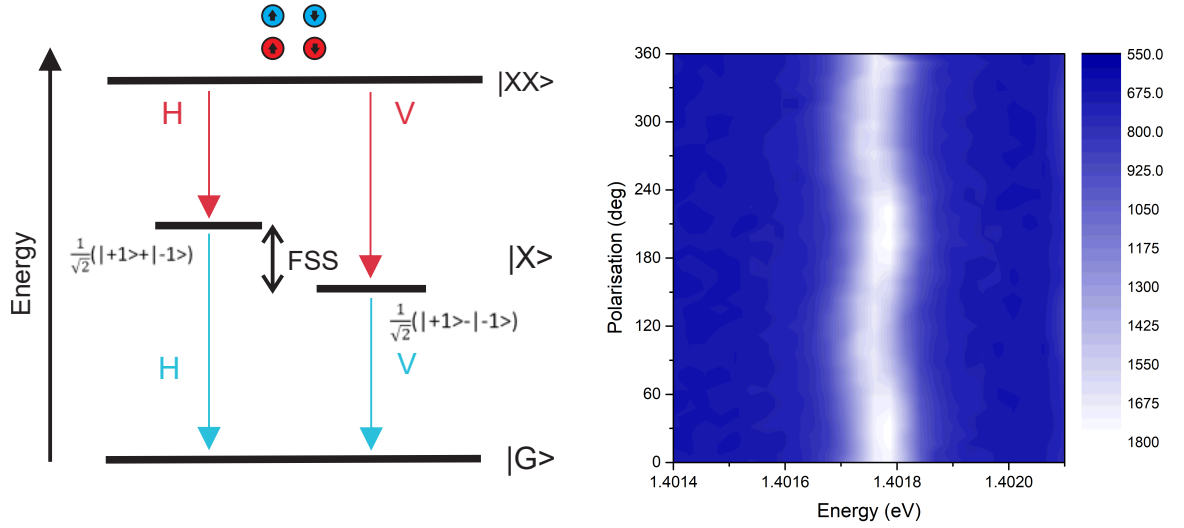


Figure 2.3.: Height profile (red) of a droplet-etched nanohole in an AlGaAs layer is shown in the left image. The orange line represents the wavefunction of the exciton which resembles the ground state of an hydrogen atom. Because of that the Bohr radius r_{Bohr} is denoted. The right image shows the atomic force microscopy picture of the nanohole. An GaAs quantum dot is obtained after filling the hole with GaAs and avergrowth with AlGaAs [4]

2.2. Fine structure splitting

Fine structure splitting (FSS) in a QD describes the energy splitting between the two possible bright $|X\rangle$ states. In GaAs it originates from the exchange interaction between electrons and holes. [5].

In figure 2.4a the $|XX\rangle$ decay path with splitted $|X\rangle$ eigenstates is shown. $|XX\rangle$ exhibit no splitting as the angular momentum of the electrons and holes add to zero and therefore no exchange interaction occurs. In figure 2.4b photoluminescence spectra recorded with a linear polarizer are shown.



(a) XX decay cascade without X degeneracy because of fine structure splitting. [1] (b) Photoluminescence spectra of X emission of a GaAs Qd plotted for different polarizer angles. In the image the effect of the linear polarization of the fine structure components is visible. [6]

Figure 2.4.: Fine structure splitting in a GaAs quantum dot.

2.3. Zero-phonon line and phonon sideband

The excitonic emission of GaAs QDs exhibit non-Lorentzian asymmetric broadening. As shown by Peter et al. [7] this side bands can be traced back to a coupling to acoustic phonons. The discussion of phonon side bands (PSBs) is based on Friedrich and Haarer [8] and Peter et al. [7].

Figure 2.5 displays a schematic representation of the zero phonon line (ZPL) and PSB absorption spectrum. The intensity distribution between the two components depends strongly on temperature.

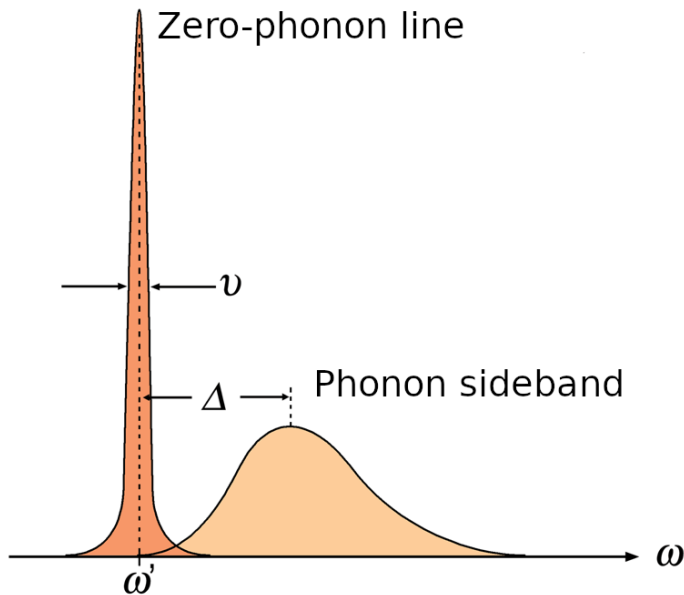
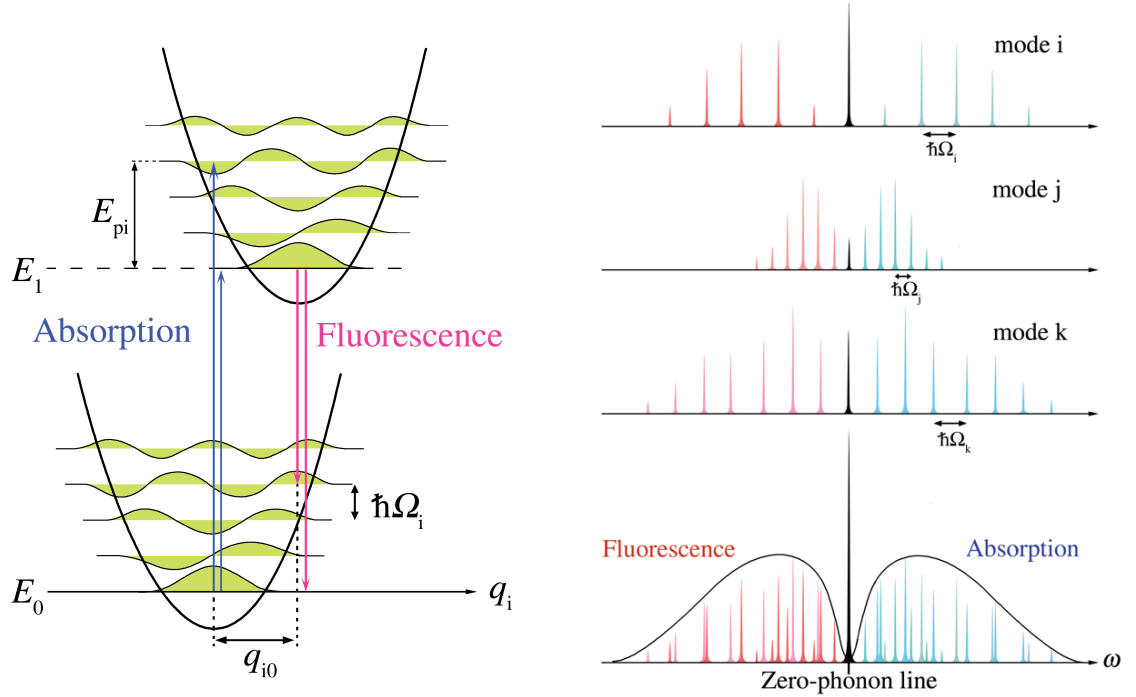


Figure 2.5.: Absorption line shape of an electronic excitation. The emission is mirrored at ω' .

To determine the frequency gap Δ the Franc-Condon principles are used. They state that electronic transition between ground and excited state is much faster than the motion in the lattice. Hence, there is no motion along the configurational coordinates q_i during the energy transitions as depicted in figure 2.6a. The transitions can be displayed as vertical arrows with the shorter arrow describing the ZPL and the longer one describing the PSB. According to the Franc-Condon principles, the more the wave functions of two vibrational energy levels overlap, the likelier is the electronic transition between these two. In the case of figure 2.6a this occurs when the photon energy equals to the energy difference $E_1 - E_0$ plus three quanta of vibrational energy $\hbar\Omega_i$. The emission follows the same principle.



(a) Energy spectrum of a two-level electronic system with phonon coupling. The arrows describe emission/absorption with and without phonons respectively.

(b) Three lattice normal modes (i, j, k) and the resulting emission/absorption spectrum.

Figure 2.6.: Zero-phonon line and phonon sideband. [9]

Figure 2.6a and 2.6b implicitly assume approximations in addition to the Franck-Condon principles. The lattice vibrational mode has to be well described by a quantum harmonic oscillator. Additionally, it is assumed that only the lowest lattice vibration is excited and that the harmonic oscillator potentials are equal in both states. These preconditions are visible in the equally parabolic shaped potential wells and equally spaced phonon energy levels in figure 2.6a.

The zero-phonon line is stronger than the phonon side band because of the superposition of the lattice modes. Each lattice mode m lead to a different energy difference $\hbar\Omega_m$ between phonons. That is why the transitions with phonons result in a energy distribution and the zero-phonon transition add at the electronic origin $E_1 - E_0$.

The theoretical limit of the spectral range of the zero-phonon line for a GaAs quantum dot can be calculated with the time-energy uncertainty relation

$$\Delta E \cdot \Delta t = \frac{h}{2\pi} \quad (2.1)$$

This gives for typical lifetime of a GaAs quantum dot of $\Delta t = 250 \text{ ps}$

$$\Delta E = 2.64 \mu\text{eV}. \quad (2.2)$$

The frequency uncertainty can be obtained through

$$\Delta\nu = \frac{\Delta E}{h}. \quad (2.3)$$

The wavelength λ relates to ν with the Planck-Einstein relation

$$\lambda(\nu) = \frac{c}{\nu} \quad (2.4)$$

and the wavelength uncertainty $\Delta\lambda$ can be approximated with a Taylor series around ν_0

$$\Delta\lambda = -\lambda'(\nu_0) \cdot \Delta\nu. \quad (2.5)$$

With equation (2.3) and the center wavelength of the zero-phonon line λ_0 in table 2.1 this gives

$$\Delta\lambda = \frac{c}{\nu_0^2} \cdot \Delta\nu = \frac{\lambda_0^2}{c} \cdot \Delta\nu \quad (2.6)$$

$$\approx 1.0 \text{ pm} \quad (2.7)$$

Reorganize

Table 2.1.: Parameters of GaAs quantum dots used in the laboratory of semiconductor physics department in Linz. Zero-phonon line calculates from the theoretical limit according to the life time of the excitonic state (as can be seen in equation (2.7)) up to broader lines which are still valued enough to be measured. The phonon sideband resembles data taken from Schöll et al. [10].

Quantum dot emission	Center wavelength λ_0	Spectral range $\Delta\lambda$	Waveform
Zero-phonon line	(700 to 800) nm	(1.0 to 1.4) pm	Cauchy
Phonon sideband	~0.25 nm higher than zero-phonon line	500 pm	Gauss

The zero-phonon line is described with a Cauchy distribution

$$\Phi_{dot,zero}(\lambda) = \frac{1}{\pi \cdot \Delta\lambda_{zero} \cdot 0.5 \left[1 + \left(\frac{\lambda - \lambda_{0,zero}}{\Delta\lambda_{zero} \cdot 0.5} \right)^2 \right]} \quad (2.8)$$

with $\lambda_{0,zero}$ as the center wavelength and $\Delta\lambda_{zero}$ as the spectral range of the zero-phonon line.

The phonon side band is described with a Gauss distribution

$$\Phi_{dot,side}(\lambda) = \frac{1}{\sqrt{2 \cdot \pi \cdot \Delta\lambda_{side}^2}} \cdot \exp \left(-\frac{(\lambda - \lambda_{0,side})^2}{2 \cdot \Delta\lambda_{side}^2} \right) \quad (2.9)$$

2. Droplet etched gallium arsenide quantum dots

with $\lambda_{0,side}$ as the center wavelength and $\Delta\lambda_{side}$ as the spectral range of the phonon side band.

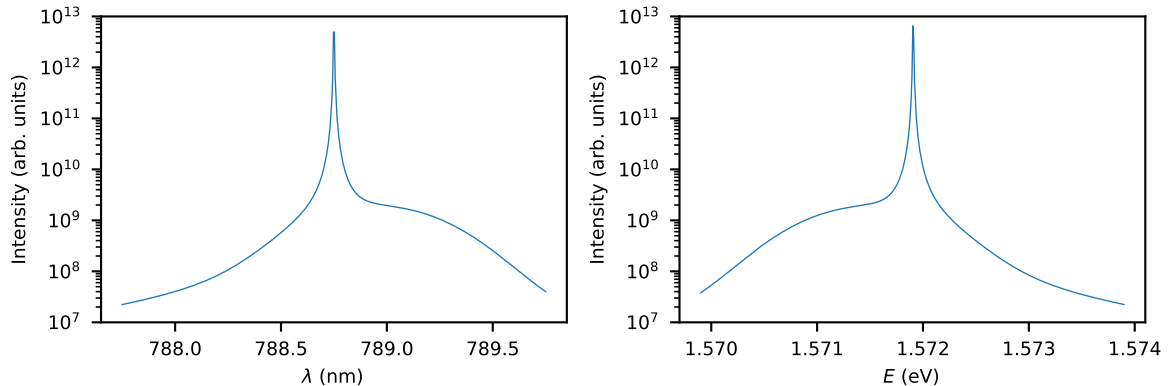


Figure 2.7.: Simulated exciton emission of a GaAs quantum dot plotted dependant on the wavelength λ and the Energy E . The parameters can be found in table 2.1.

2.4. Optical excitation of a quantum dot

Dot-Spectra
in far field is
(TEM_{00}).

2.5. Resonant two-photon excitation

2.6. Single photon emission

3. Single photon generation using adiabatic rapid passage with frequency-chirped pulses

3.1. Introduction and motivation

3.2. Fundamentals of chirp and interferometric autocorrelation

3.2.1. Chirp

3.2.2. Interferometric autocorrelation

3.2.3. Modified-spectrum autointerferometric correlation

3.3. Adiabatic rapid passage

3.4. Simulation

3.5. Measurements and discussion

4. Building up a scanning Fabry-Pérot interferometer from scratch

4.1. Introduction and motivation

The Fabry Pérot interferometer (FPI) is an optical resonator developed by Charles Fabry and Alfred Pérot. An incoming light beam will only be transmitted through the resonator consisting of two semi-transparent mirrors if it fulfils the resonance condition.[11]

Goal: Resolve
QD emission
line.

4.2. Transverse modes of electromagnetic radiation

4.2.1. Gaussian beam

In this subsection, light beams are described by the wave picture according to Meschede [12]. They fulfil the Maxwell equations and therefore their electric field $\mathbf{E}(\mathbf{r}, t)$ fulfils the wave equation

$$\left(\nabla^2 - \frac{1}{c^2} \frac{\partial}{\partial t^2} \right) \mathbf{E}(\mathbf{r}, t) = 0. \quad (4.1)$$

Along the propagation direction z a light beam behaves similarly to a plane wave with constant amplitude A_0 which is a known solution to the wave equation (4.1)

$$E(z, t) = A_0 e^{-i(\omega t - kz)}. \quad (4.2)$$

However, far from its source light is expected to behave like a spherical wave

$$E(\mathbf{r}, t) = A_0 \frac{e^{-i(\omega t - \mathbf{k}\mathbf{r})}}{|\mathbf{k}\mathbf{r}|}. \quad (4.3)$$

4. Building up a scanning Fabry-Pérot interferometer from scratch

To get a better understanding of the propagation of light, only paraxial (near the z-axis) parts of the spherical wave are considered. Additionally, the wave is split into its longitudinal (z-axis) part and its transversal part and beams with axial symmetry are assumed, which only depend on a transversal coordinate ρ . Under these circumstances \mathbf{kr} can be replaced with kr and because of $\rho \ll r, z$ the Fresnel approximation can be applied:

$$E(\mathbf{r}) = \frac{A(\mathbf{r})}{|\mathbf{kr}|} e^{i\mathbf{kr}} \simeq \frac{A(z, \rho)}{kz} \exp\left(i\frac{k\rho^2}{2z}\right) e^{ikz} \quad (4.4)$$

with $r = \sqrt{z^2 + \rho^2} \simeq z + \rho^2/2z$.

Equation (4.4) resembles the plain wave in equation (4.2), with the spacial phase transversally modulated by $\exp(ik\rho^2/2z)$. Another spherical wave solution can be obtained by applying the following replacement (z_0 is a real number)

$$z \rightarrow q(z) = z - iz_0. \quad (4.5)$$

Thereby, the fundamental (or TEM₀₀) Gaussian mode has been constructed

$$E(z, \rho) \simeq \frac{A_0}{kq(z)} \exp\left(i\frac{k\rho^2}{2q(z)}\right) e^{ikz}. \quad (4.6)$$

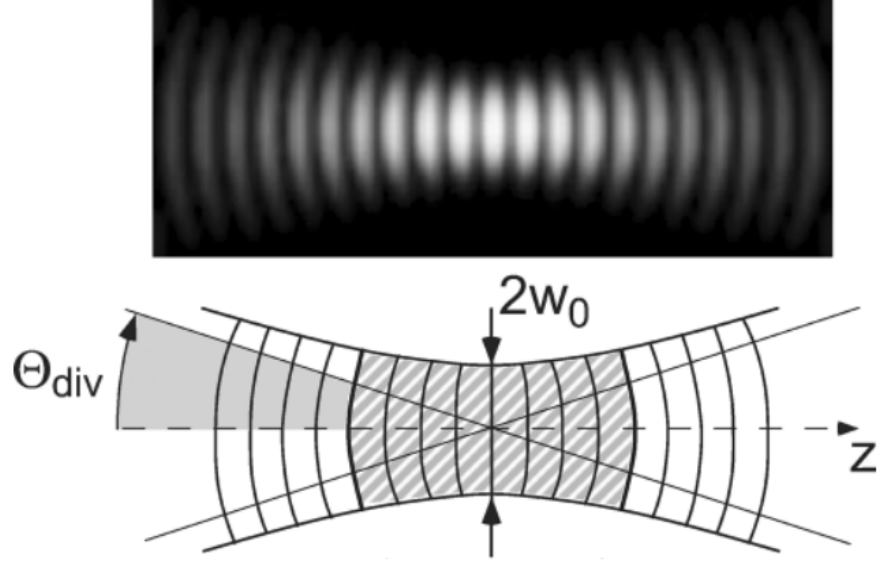


Figure 4.1.: A Gaussian beam near its beam waist. Near the center they resemble plan wave fronts, while outside they converge towards spherical wave fronts. Their Rayleighzone is shaded at the lower part of the figure.[12]

The electrical and magnetical fields of gauss modes are transversal to its propagation direction. These waveforms are called transversal elctrical and magnetic modes with indices (m, n) . Its fundamental solution is the TEM₀₀-Mode, which is the most important one and will therefore be examined in more detail in the rest of this subsection.

By executing the replacement $q(z) \rightarrow z - iz_0$ explicitly the equation (4.6) can be expressed as

$$\frac{1}{q(z)} = \frac{z + iz_0}{z^2 + z_0^2} = \frac{1}{R(z)} + i \frac{2}{k\omega^2(z)}, \quad (4.7)$$

with new variables z_0 , $R(z)$ and $\omega(z)$ being introduced. With the decomposition of the Fresnel factors into real and imaginary part, two factors can be identified: one complex phase factor, which describes the curvature of the wavefronts and a real factor, which describes the envelope of the beam. Therefore, the exponential in equation (4.6) becomes

$$\exp\left(i \frac{k\rho^2}{2q(z)}\right) \rightarrow \exp\left(i \frac{k\rho^2}{2R(z)}\right) \exp\left(-\left(\frac{\rho}{\omega(z)}\right)^2\right) \quad (4.8)$$

For the following description of gauss modes the following parameters have to be introduced

- **Evolving radius of curvature $R(z)$:**

$$R(z) = z(1 + (z_0/z)^2) \quad (4.9)$$

- **Beam waist $2\omega_0$:**

$$\omega_0^2 = \lambda z_0 / \pi \quad (4.10)$$

The beam waist $2\omega_0$ or beam radius ω_0 describe the smallest beam cross section at $z = 0$. If the wave propagates inside a medium with the refractive index n , λ has to be replaced with λ/n . The cross section of the beam waist is then $\omega_0^2 = \lambda z_0 / (\pi n)$.

A Gaussian beam can be completely characterized at every point z on the beam axis either with the parameter couple (ω_0, z_0) or alternatively with the real and imaginary part of $q(z)$. The parameters of the Gaussian beam are transformed by linear operations, which coefficients are identical to those from geometrical optics

$$q_{out} = \frac{Aq_{in} + B}{Cq_{in} + D} \quad (4.11)$$

with the parameters A, B, C, D determined by the optical element transforming the Gaussian beam described by q_{in} .

4.2.2. Higher Gauss modes

The wave equation (4.1) can be simplified, by only allowing monochromatic waves with harmonic time dependence

$$\mathbf{E}(\mathbf{r}, t) = \text{Re} \left(\mathbf{E}(\mathbf{r}) e^{-i\omega t} \right). \quad (4.12)$$

With $\omega^2 = c^2 \mathbf{k}^2$, the *Helmholtz equation* can be deduced, which only depends on the location \mathbf{r}

$$(\nabla^2 + \mathbf{k}^2) \mathbf{E}(\mathbf{r}) = 0. \quad (4.13)$$

In favour of a formal treatment of the Gaussian modes, the Helmholtz equation is splitted into its transversal and longitudinal contribution,

$$\nabla^2 + k^2 = \frac{\partial^2}{\partial z^2} + \nabla_T^2 + k^2 \quad \text{with} \quad \nabla_T^2 = \frac{\partial}{\partial x^2} + \frac{\partial}{\partial y^2}, \quad (4.14)$$

and apply it on the electric field of equation (4.4). It is assumed that the amplitude A only changes slowly in the order of the wavelength,

$$\frac{\partial}{\partial z} A = A' \ll kA, \quad (4.15)$$

which allows the approximation

$$\frac{\partial^2}{\partial z^2} A e^{ik\rho^2/(2z)} \frac{e^{ikz}}{kz} \simeq (2ikA' - k^2 A) e^{ik\rho^2/(2z)} \frac{e^{ikz}}{kz}, \quad (4.16)$$

and results in the *paraxial Helmholtz equation*,

$$\left(\nabla_T^2 + 2ik \frac{\partial}{\partial z} \right) A(\rho, z) = 0. \quad (4.17)$$

The fundamental solution is the TEM₀₀ mode in equation (4.6). Examples of higher modes can be found in figure 4.2.

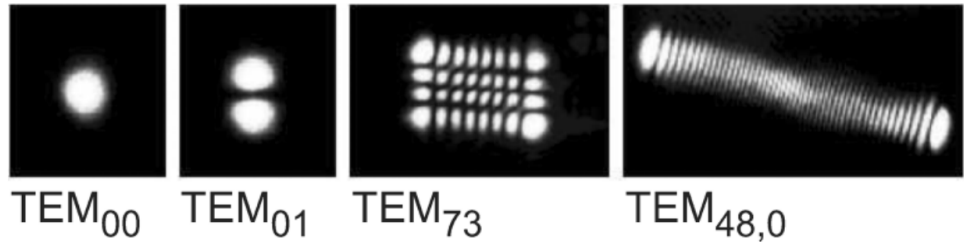


Figure 4.2.: Gaussian modes higher order of a simple Ti-sapphire laser. The asymmetry of the high modes are caused by technical inaccuracies of the resonator elements (mirrors, laser crystal).

4.3. Fundamentals of Fabry-Pérot interferometers

4.3.1. Resonator losses

For the following discussion of the FPI, a two-mirror-resonator with the reflecting surfaces facing each other and air as medium in between is assumed. The theoretical foundation is provided by the work of Ismail et al. [13].

The time the light needs for one roundtrip is given by

$$t_{RT} = \frac{2l}{c} \quad (4.18)$$

where l is the geometrical length of the resonator and c is the speed of light in air.

The photon-decay time τ_c of the interferometer is then given by

$$\frac{1}{\tau_c} = -\frac{\ln(R_1 \cdot R_2)}{t_{RT}} \quad (4.19)$$

where R_1 and R_2 are the corresponding intensity reflectivities of the mirrors.

The number of photons at frequency ν inside the resonator is described by the differential rate equation

$$\frac{d}{dt} \varphi(t) = -\frac{1}{\tau_c} \varphi(t). \quad (4.20)$$

With a number φ_s of photons at $t = 0$ the integration gives

$$\varphi(t) = \varphi_s e^{-t/\tau_c} \quad (4.21)$$

4.3.2. Resonance frequencies, free spectral range and spectral line shapes

The round-trip phase shift at frequency ν is given by

$$2\phi(\nu) = 2\pi\nu t_{RT} = 2\pi\nu \frac{2l}{c} \quad (4.22)$$

where $\phi(\nu)$ is the single-pass phase shift between the mirrors.

Resonances are visible for frequencies ν at which the light interferes constructively after one round trip. Two adjacent resonance frequencies differ in their round trip phase shift by 2π . Hence, the free

4. Building up a scanning Fabry-Pérot interferometer from scratch

spectral range $\Delta\nu_{FSR}$, the frequency difference between two adjacent resonance frequencies, can be calculated from equation (4.28)

$$2\Delta\phi_{FSR} = 2\pi \quad (4.23)$$

$$\Rightarrow 2\pi\Delta\nu_{FSR} \frac{2l}{c} = 2\pi \quad (4.24)$$

$$\Rightarrow \Delta\nu_{FSR} = \frac{c}{2l} \quad (4.25)$$

According to equation (4.21) the number of photons decay with the photon-decay time τ_c . With $E_{q,s}$ representing the initial amplitude, the electric field at ν_q can be given by

$$E_q(t) = \begin{cases} E_{q,s} \cdot e^{i2\pi\nu_q t} \cdot e^{-t/(2\tau_c)} & t \geq 0 \\ 0 & t < 0 \end{cases}. \quad (4.26)$$

The Fourier transformation of the electric field can be expressed as

$$\tilde{E}_q(\nu) = \int_{-\infty}^{\infty} E_q(t) e^{-i2\pi\nu t} dt = E_q(t) \int_0^{\infty} e^{[1/(2\tau_c) + i2\pi(\nu - \nu_q)]t} dt = E_{q,s} \frac{1}{(2\tau_c)^{-1} + i2\pi(\nu - \nu_q)}. \quad (4.27)$$

The normalized spectral line shape per unit frequency is then given by

$$\tilde{\gamma}_q(\nu) = \frac{1}{\tau_c} \left| \frac{\tilde{E}_q(\nu)}{E_{q,s}} \right|^2 = \frac{1}{\tau_c} \left| \frac{1}{(2\tau_c)^{-1} + i2\pi(\nu - \nu_q)} \right|^2 = \frac{1}{\tau_c} \frac{1}{(2\tau_c)^{-2} + 4\pi^2(\nu - \nu_q)^2} \quad (4.28)$$

$$= \frac{1}{\pi} \frac{1/(4\pi\tau_c)}{1/(4\pi\tau_c)^2 + (\nu - \nu_q)^2} \quad (4.29)$$

with $\int \tilde{\gamma}_q(\nu) d\nu = 1$. By defining the full-width-at-half-maximum linewidth (FWHM) $\Delta\nu_c$ we get

$$\Delta\nu_c = \frac{1}{2\pi\tau_c} \Rightarrow \tilde{\gamma}_q(\nu) = \frac{1}{\pi} \frac{\Delta\nu_c/2}{(\Delta\nu_c/2)^2 + (\nu - \nu_q)^2} \quad (4.30)$$

By normalizing the Lorentzian lines so that the peak is at unity we finally obtain

$$\gamma_{q,L}(\nu) = \frac{\pi}{2} \Delta\nu_c \tilde{\gamma}_q(\nu) = \frac{(\Delta\nu_c)^2}{(\Delta\nu_c)^2 + 4(\nu - \nu_q)^2} \quad (4.31)$$

with $\gamma_{q,L}(\nu_q) = 1$.

4.3.3. Airy distribution of Fabry-Pérot interferometers

The response of the FPI is calculated with the circulating-field approach [13], where a steady-state is assumed. E_{circ} is the result of E_{laun} interfering with E_{RT} . E_{laun} is the transmission of the incoming light

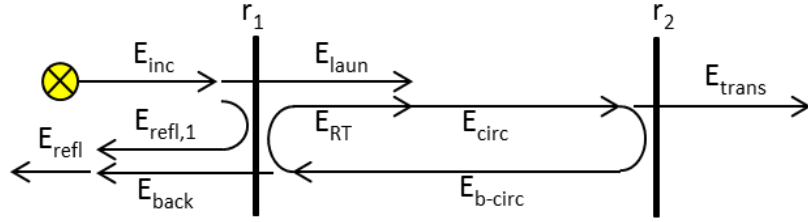


Figure 4.3.: FPI with electric field mirror reflectivities r_1 and r_2 . Indicated in this figure are the electric fields resulting from an incoming E_{inc} , the reflected field $E_{refl,1}$ and transmitted field E_{laun} . E_{circ} and $E_{circ,b}$ circulate inside the resonator, resulting in E_{RT} after one round-trip. E_{back} is the backwards transmitted field.[14]

E_{inc} and E_{RT} is E_{circ} after one round-trip in the resonator, i.e., after the outcoupling losses of mirror 1 and 2. Therefore, the field E_{circ} can be calculated from E_{laun} by

$$E_{circ} = E_{laun} + E_{RT} = E_{laun} + r_1 r_2 e^{-i2\phi} E_{circ} \Rightarrow \frac{E_{circ}}{E_{laun}} = \frac{1}{1 - r_1 r_2 e^{-i2\phi}} \quad (4.32)$$

where r_1 and r_2 are the electric-field reflectivities of mirror 1 and 2.

The generic Airy distribution considers only light inside the mirrors and is defined as

$$A_{circ} = \frac{I_{circ}}{I_{laun}} = \frac{|E_{circ}|^2}{|E_{laun}|^2} = \frac{1}{|1 - r_1 r_2 e^{-i2\phi}|^2} = \frac{1}{(1 - \sqrt{R_1 R_2})^2 + 4\sqrt{R_1 R_2} \sin^2(\phi)} \quad (4.33)$$

by using

$$\begin{aligned} |1 - r_1 r_2 e^{-i2\phi}|^2 &= |1 - r_1 r_2 \cos(2\phi) + ir_1 r_2 \sin(2\phi)|^2 = [1 - r_1 r_2 \cos(2\phi)]^2 + r_1^2 r_2^2 \sin^2(2\phi) \\ &= 1 + R_1 R_2 - 2\sqrt{R_1 R_2} \cos(2\phi) = (1 - \sqrt{R_1 R_2})^2 + 4\sqrt{R_1 R_2} \sin^2(\phi) \end{aligned}$$

and additionally $R_i = r_i^2$ and $\cos(2\phi) = 1 - 2\sin^2(\phi)$.

Commonly, light is sent through the FPI. Therefore the following sections will use the Airy distribution A'_{trans} .

$$A'_{trans} = \frac{I_{trans}}{I_{inc}} = \frac{I_{circ} \cdot (1 - R_2)}{I_{laun} / (1 - R_1)} = (1 - R_1)(1 - R_2) A_{circ} = \frac{(1 - R_1)(1 - R_2)}{(1 - \sqrt{R_1 R_2})^2 + 4\sqrt{R_1 R_2} \sin^2(\phi)} \quad (4.34)$$

A'_{trans} is displayed in figure 4.4 for $R_1 = R_2$. The peak value at one of its resonance frequencies calculates as follows

$$A'_{trans} = \frac{(1 - R_1)(1 - R_2)}{(1 - \sqrt{R_1 R_2})^2} \stackrel{R_1=R_2}{=} 1. \quad (4.35)$$

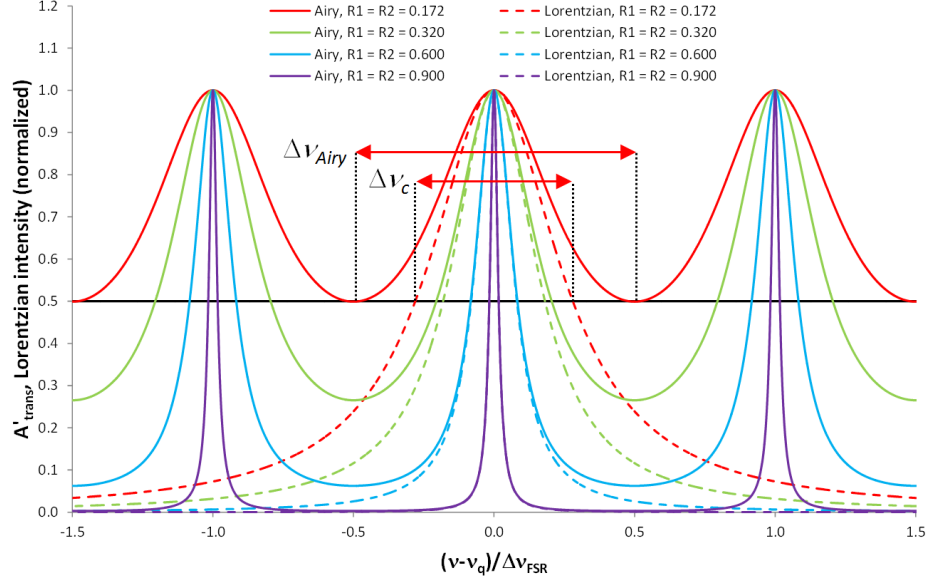


Figure 4.4.: Airy distribution A'_{trans} as described in equation (4.34) compared to the Lorentzian lines $\gamma_{q,L}$ as described in equation (4.31)

4.3.4. Airy linewidth and finesse

The airy linewidth is defined as the full width at half maximum (FWHM) of A'_{trans} . It can be set in relation with the free spectral range $\Delta\nu_{FSR}$ and the mirror reflectivities as follows.

A'_{trans} decreases to half of its peak value at $A'_{trans}(v_q)/2$ when the phase shift ϕ changes by the amount $\Delta\phi$ so that the denominator of A'_{trans} in equation (4.34) is twice as big

$$\left(1 - \sqrt{R_1 R_2}\right)^2 = 4\sqrt{R_1 R_2} \sin^2(\Delta\phi) \quad (4.36)$$

$$\Rightarrow \Delta\phi = \arcsin\left(\frac{1 - \sqrt{R_1 R_2}}{2\sqrt[4]{R_1 R_2}}\right) \quad (4.37)$$

With equation (4.22) and (4.25), the phase shift can be expressed as

$$\phi = \frac{\pi\nu}{\Delta\nu_{FSR}} \quad (4.38)$$

$$\Rightarrow \Delta\phi = \frac{\pi(\Delta\nu_{Airy}/2)}{\Delta\nu_{FSR}}. \quad (4.39)$$

Therefore, with equation (4.37) and (4.39) the FWHM linewidth is given by

$$\Delta\nu_{Airy} = \Delta\nu_{FSR} \frac{2}{\pi} \arcsin\left(\frac{1 - \sqrt{R_1 R_2}}{2\sqrt[4]{R_1 R_2}}\right). \quad (4.40)$$

The finesse of the Airy distribution of a FPI is defined as

$$F_{\text{Airy}} := \frac{\Delta\nu_{\text{FSR}}}{\Delta\nu_{\text{Airy}}} = \frac{\pi}{2} \left[\arcsin \left(\frac{1 - \sqrt{R_1 R_2}}{2 \sqrt[4]{R_1 R_2}} \right) \right]^{-1} \quad (4.41)$$

and is therefore only dependent on the mirror reflectivities R_1 and R_2 .

The Airy finesse is the determining property when it comes to the spectral resolution of the FPI. This can be made visible by comparing its message with the Taylor criterion for the resolution of two adjacent peaks. The Taylor criterion proposes that two spectral lines are resolvable when the separation of the maxima is greater than the FWHM. As displayed in figure 4.5, the Airy finesse is equal to the number of Airy distributions originating from light at certain frequencies ν_m which do not overlap at a point higher than half of their maxima. Hence, the Airy finesse describes the spectral resolution in a way that is consistent with the Taylor criterion.

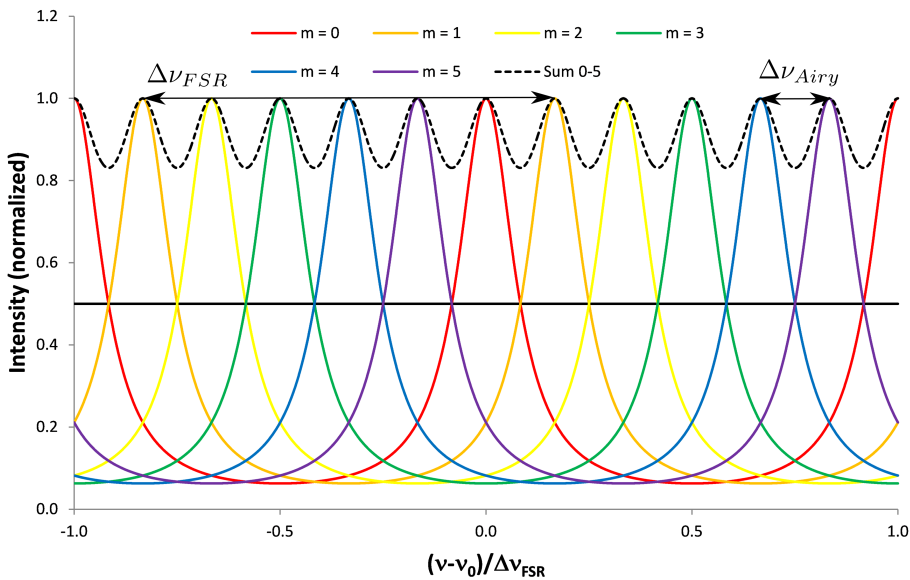


Figure 4.5.: Demonstration of the physical meaning of the Airy finesse F_{Airy} . The coloured lines are Airy distributions created by light at distinct frequencies ν_m , while scanning the resonator length. When the light occurs at frequencies $\nu_m = \nu_q + m\Delta\nu_{\text{Airy}}$, the adjacent Airy distributions are separated from each other by ν_{Airy} , therefore fulfilling the Taylor criterion. Since in this example $F_{\text{Airy}} = 6$ exactly six peaks fit inside the free spectral range. As can be seen in the figure the Airy finesse F_{Airy} quantifies the maximum number of peaks that can be resolved. [14]

4.3.5. Mode matching and spatial filtering

One fundamental challenge of Fabry Pérot interferometry is how to efficiently couple an incident beam of light into a given mode of the resonator. The following discussion is based on the work of Yariv, Yeh, and Yariv [15] and Meschede [12].

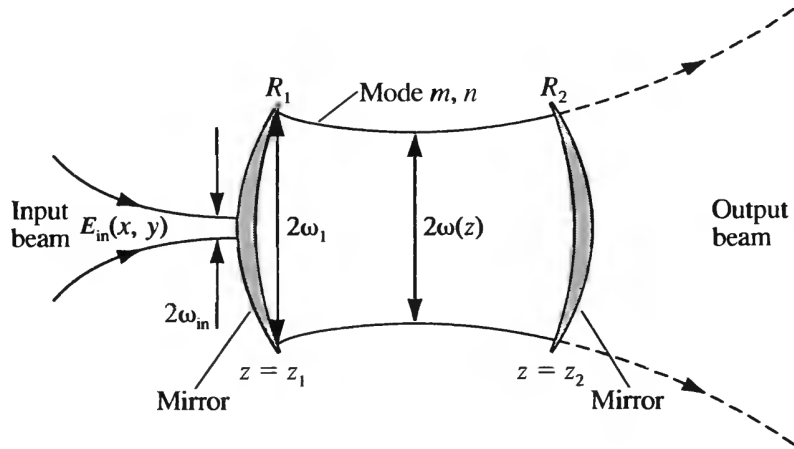


Figure 4.6.: Incident monochromatic beam of light exciting transverse mode m, n of a resonator [15]

In accordance with figure 4.6, an input beam E_{in} propagates into the resonator and potentially excite its modes $E_{mn}(x, y)$, where m, n are the transverse mode integers of the Gaussian beam of the optical resonator. Since $E_{mn}(x, y)$ describes a complete orthogonal set of wavefunctions they satisfy

$$\iint E_{mn}(x, y) E_{m'n'}^*(x, y) dx dy = 0 \quad \text{unless } m = m' \text{ and } n = n'. \quad (4.42)$$

and

$$E_{in}(x, y) = \sum_{mn} a_{mn} E_{mn}(x, y) \quad (4.43)$$

where a_{mn} are constants. By multiplying both sides of equation (4.43) with E_{mn}^* , integrating over the whole x - y -plane and using equation (4.42), the following expression can be obtained

$$a_{mn} = \frac{\iint E_{in}(x, y) E_{mn}^*(x, y) dx dy}{\iint E_{mn}(x, y) E_{mn}^*(x, y) dx dy} \quad (4.44)$$

The efficiency of coupling an incident field into a spatial mode E_{mn} is defined as

$$\eta_{mn} = \frac{\text{Power coupled into mode } mn}{\text{Total incident power}} = \frac{\iint |a_{mn} E_{mn}(x, y)|^2 dx dy}{\iint |E_{in}(x, y)|^2 dx dy}. \quad (4.45)$$

By inserting equation (4.44) into equation (4.45) the following expression can be obtained

$$\eta_{mn} = \frac{|\iint E_{in}(x,y)E_{mn}^*(x,y)dx dy|^2}{\iint |E_{in}(x,y)|^2 dx dy \cdot \iint |E_{mn}(x,y)|^2 dx dy}. \quad (4.46)$$

From equation (4.46) can be deduced, that for an input beam with the *same* spatial dependency as the mode to be excited

$$E_{in}(x,y) \sim E_{mn}(x,y) \quad (4.47)$$

all of the incident power goes into E_{mn} , i.e. $\eta_{mn} = 1$ and all other $\eta_{m'n'}$ are zero. Usually the fundamental TEM₀₀ mode is desired and equation (4.46) implies that a pure Gaussian beam excites only the fundamental mode and the interferometer will then irradiate a pure Gaussian beam as well. In practise, additional measures are necessary such as matching the radius of curvature by Gaussian beam focusing.

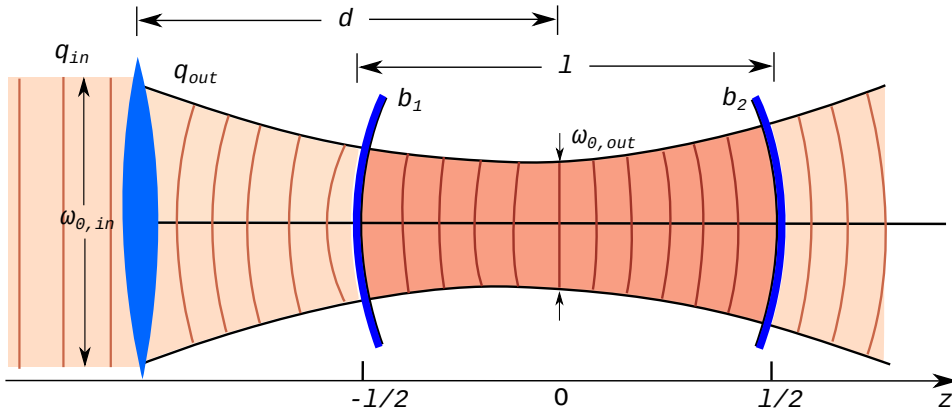


Figure 4.7.: Mode matching of an Gaussian beam into a Fabry Pérot interferometer. Incoming Gaussian beam described by q_{in} transformed by a lens into a Gaussian beam described by q_{out} . The parameters b_1 and b_2 describe the radii of the two mirrors.

In order to match the radius of curvature of the incoming Gaussian beam with the radius of curvature of the resonator a lens is inserted as depicted in figure 4.7. Light with a beam waist of ω_{01} gets focused into the resonator. Transformations by thin lenses can be described with the ABCD-rule introduced in subsection 4.2.1:

$$\begin{pmatrix} A & B \\ C & D \end{pmatrix} = \begin{pmatrix} 1 & 0 \\ \frac{-1}{f} & 1 \end{pmatrix} \quad (4.48)$$

with f as the wavelength of the lens. The incoming beam described by q_{in} is transformed by the lens into a beam described by q_{out} according to equation (4.10) and (4.11)

$$q_{in} = z + i \frac{\pi n \omega_{0,in}^2}{\lambda} \quad \text{and} \quad q_{out} = \frac{q_{in}}{q_{in} \cdot \frac{-1}{f} + 1} = z + i \frac{\pi n \omega_{0,out}^2}{\lambda} \quad (4.49)$$

4. Building up a scanning Fabry-Pérot interferometer from scratch

with $n \approx 1$ for air. Together with equation (4.10) to following relation can be deduced

$$\omega_{0,out}^2 = \frac{\omega_{0,in}^2}{\left(1 - \frac{z}{f}\right)^2 + \left(\frac{\pi\omega_{0,in}}{\lambda f}\right)^2} \quad (4.50)$$

The radii of curvature have to match. For given mirrors (described by R_{mirror}) and lens (described by f) the input beam waist has to be adjusted according to equation (4.9) and (4.10)

$$R_{mirror} \stackrel{!}{=} R_{gauss}(z = l/2) \quad (4.51)$$

$$R_{mirror} \stackrel{!}{=} \frac{l}{2} \left(1 + \left(\frac{2z_{0,out}}{l}\right)^2\right) \quad (4.52)$$

$$R_{mirror} \stackrel{!}{=} \frac{l}{2} \left(1 + \left(\frac{2\omega_{0,out}^2 \pi}{l\lambda}\right)^2\right). \quad (4.53)$$

Inserting equation (4.53) into equation (4.50) results in the condition for mode matching

$$R_{mirror} = \frac{l}{2} \left(1 + \left(\frac{2\omega_{0,in}^2 \pi}{\left(\left(1 - \frac{z}{f}\right)^2 + \left(\frac{\pi\omega_{0,in}}{\lambda f}\right)^2\right) l\lambda}\right)^2\right). \quad (4.54)$$

One way to further suppress higher modes is *spatial filtering*. It can be seen in figure 4.2 that the effective area of a mode increases with its order (m, n). Figure 4.8 shows one way to suppress higher modes consisting of a focusing lens and a pin hole which diameter TEM₀₀ mode.

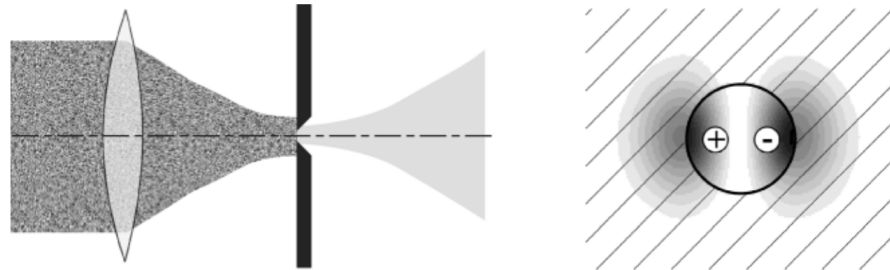


Figure 4.8.: Spatial filtering of Gauss modes. In front of the aperture, the beam consists of a superposition of multiple Gauss modes. In the example of TEM₀₁ is displayed, how higher modes are suppressed by the aperture. [12]

4.3.6. Confocal setup

If the incoming beam would represent a perfect TEM₀₀ mode, spatial filtering would not be necessary and mode matching wouldn't have to be done as precise. Unfortunately, this can not always be

guaranteed and mode matching plus spatial filtering is tedious and error prone. Arranging the mirrors of a FPI into a confocal arrangement reduces the need for these measures. By giving up the ability to choose different free spectral ranges with a given pair of mirrors, the confocal setup liberates from mode matching considerations as the cavity is mode degenerate, i.e the frequency of certain axial and transverse cavity modes are the same. The following discussion is based on Hercher [16].

A quasi-monochromatic beam of wavelength λ_0 is composed of transverse modes TEM_{mnq} , where the subscripts m and n denote the amplitude distribution of the normal mode on a surface of constant phase and q the number of axial modes inside the resonator. Each of these modes resonates for mirror separations satisfying

$$l = \frac{\lambda_0}{2} \{q + (1 + m + n) \cos^{-1} [(1 - l/b_1)(1 - l/b_2)]^{1/2}\} \quad (4.55)$$

where the parameters b_1 and b_2 describe the radii of the two mirrors as can be seen in figure 4.7.

For the confocal setup $l = b_1 = b_2$ which justifies the approximation

$$l \approx \frac{\lambda_0}{2} [q + (1 + m + n)]. \quad (4.56)$$

The modes resonate at mirror separations of either

$$l = \frac{\lambda_0}{2}(p + 1) \quad p \in \mathbb{N} \text{ and } (m + n) \text{ even,} \quad (4.57)$$

$$l = \frac{\lambda_0}{2}(p) \quad p \in \mathbb{N} \text{ and } (m + n) \text{ odd.} \quad (4.58)$$

If mode matching is not executed, it can be assumed that the incoming beam consists of an approximately equal number of even and odd transverse modes. The resonance cavity length l does not depend on n, m and q anymore but only on one integer p . The transversal modes are degenerate and fulfil

$$l = \frac{\lambda_0 p}{2}. \quad (4.59)$$

It can be additionally concluded from equation (4.59), that a change of $\lambda_0/2$ in the mirror separation scans through one free spectral range.

4.4. Simulation

The goal in building up a scanning Fabry Pérot interferometer is to resolve features of the emission spectra of GaAs quantum dots described in chapter 2. More precisely, it is intended to resolve the

4. Building up a scanning Fabry-Pérot interferometer from scratch

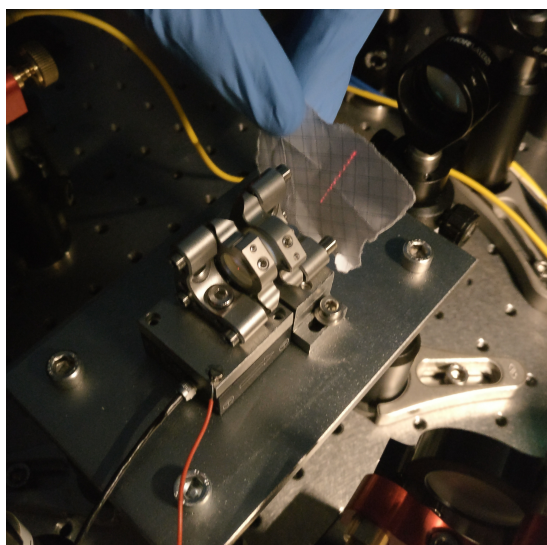
shape of the ZPL and the PSB. Equation 4.41 shows that the finesse is constant for a given pair of mirrors. When the spectrum to be resolved is broad a higher free spectral range $\Delta\nu_{FSR}$ has to be chosen, under the loss of resolution. When the spectrum contains fine details which need to be resolved a lower ν_{Airy} has to be chosen, which results in a lower free spectral range $\Delta\nu_{FSR}$. Hence, the thin ZPL and the broad PSB can not be resolved with the same setup. Instead, the mirror distances have to be adjusted and in the confocal setup discussed in subsection 4.3.6 the mirrors have to be exchanged as well.

4.5. Setup

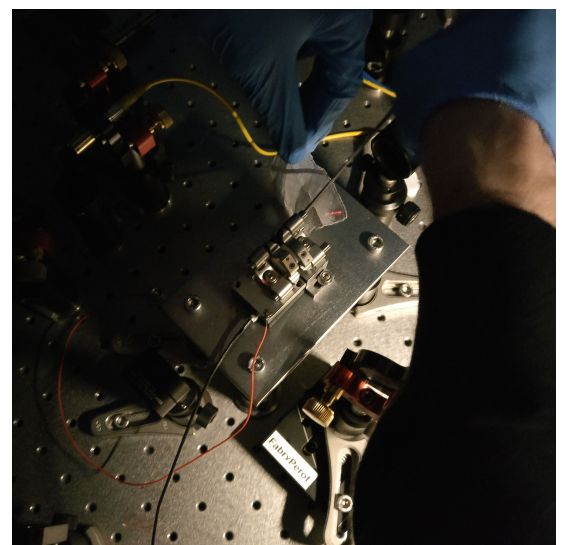
4.5.1. Flat mirrors

4.5.2. Concave mirrors

4.5.3. Confocal setup



(a)



(b)

Figure 4.9.: Fabry Pérot interferometer

4.6. Measurements and discussion

5. Summary and conclusion

6. Outlook

Appendix

Appendix A.

Acronyms

QD	quantum dot	
X	exciton	4
XX	biexciton	4
FSS	fine structure splitting	
ZPL	zero phonon line	7
PSB	phonon side band	7
GaAs	gallium arsenide	3
Al	aluminium	3
MBE	molecular beam epitaxy	3
AFM	atomic force microscopy	
FPI	Fabry P��rot interferometer	13
FWHM	full width at half maximum	20
CB	conduction band	3
VB	valence band	3

Bibliography

- [1] Daniel Huber. "GaAs quantum dots: A Dephasing-Free Source of Entangled Photon Pairs." PhD thesis. 2019 (cit. on pp. 3–6).
- [2] Zh. M. Wang et al. "Nanoholes fabricated by self-assembled gallium nanodrill on GaAs(100)." In: *Applied Physics Letters* 90.11 (Mar. 12, 2007), p. 113120. ISSN: 0003-6951, 1077-3118. DOI: 10.1063/1.2713745. URL: <http://aip.scitation.org/doi/10.1063/1.2713745> (visited on 06/13/2019) (cit. on p. 3).
- [3] R. M. Stevenson et al. "A semiconductor source of triggered entangled photon pairs." In: *Nature* 439.7073 (Jan. 2006), pp. 179–182. ISSN: 0028-0836, 1476-4687. DOI: 10.1038/nature04446. URL: <http://www.nature.com/articles/nature04446> (visited on 06/17/2019) (cit. on p. 4).
- [4] Marcus Reindl et al. "Highly indistinguishable single photons from incoherently and coherently excited GaAs quantum dots." In: *arXiv:1901.11251 [cond-mat]* (Jan. 31, 2019). arXiv: 1901.11251. URL: <http://arxiv.org/abs/1901.11251> (visited on 06/04/2019) (cit. on p. 5).
- [5] M. Bayer et al. "Fine structure of neutral and charged excitons in self-assembled In(Ga)As/(Al)GaAs quantum dots." In: *Physical Review B* 65.19 (May 7, 2002). ISSN: 0163-1829, 1095-3795. DOI: 10.1103/PhysRevB.65.195315. URL: <https://link.aps.org/doi/10.1103/PhysRevB.65.195315> (visited on 06/17/2019) (cit. on p. 6).
- [6] Christian Schimpf. "Towards quantum teleportation with remote quantum dots." PhD thesis. 2017 (cit. on p. 6).
- [7] E. Peter et al. "Phonon sidebands in exciton and biexciton emission from single GaAs quantum dots." In: *Physical Review B* 69.4 (Jan. 26, 2004), p. 041307. ISSN: 1098-0121, 1550-235X. DOI: 10.1103/PhysRevB.69.041307. URL: <https://link.aps.org/doi/10.1103/PhysRevB.69.041307> (visited on 06/11/2019) (cit. on p. 7).

Bibliography

- [8] Josef Friedrich and Dietrich Haarer. "Photochemical Hole Burning: A Spectroscopic Study of Relaxation Processes in Polymers and Glasses." In: *Angewandte Chemie International Edition in English* 23.2 (Feb. 1984), pp. 113–140. ISSN: 0570-0833, 1521-3773. DOI: 10.1002/anie.198401131. URL: <http://doi.wiley.com/10.1002/anie.198401131> (visited on 06/11/2019) (cit. on p. 7).
- [9] *Zero-phonon line and phonon sideband - Wikipedia*. URL: https://en.wikipedia.org/wiki/Zero-phonon_line_and_phonon_sideband (visited on 06/11/2019) (cit. on p. 8).
- [10] Eva Schöll et al. "Resonance fluorescence of GaAs quantum dots with near-unity photon indistinguishability." In: *Nano Letters* 19.4 (Apr. 10, 2019), pp. 2404–2410. ISSN: 1530-6984, 1530-6992. DOI: 10.1021/acs.nanolett.8b05132. arXiv: 1901.09721. URL: <http://arxiv.org/abs/1901.09721> (visited on 05/09/2019) (cit. on p. 9).
- [11] Timo Kaldewey et al. "Coherent and robust high-fidelity generation of a biexciton in a quantum dot by rapid adiabatic passage." In: *Physical Review B* 95.16 (Apr. 10, 2017). ISSN: 2469-9950, 2469-9969. DOI: 10.1103/PhysRevB.95.161302. arXiv: 1701.01371. URL: <http://arxiv.org/abs/1701.01371> (visited on 12/11/2018) (cit. on p. 13).
- [12] Dieter Meschede. *Optik, Licht und Laser*. 3., durchges. Aufl. Studium. OCLC: 254422596. Wiesbaden: Vieweg + Teubner, 2008. 568 pp. ISBN: 978-3-8351-0143-2 (cit. on pp. 13, 14, 22, 24).
- [13] Nur Ismail et al. "Fabry-Pérot resonator: spectral line shapes, generic and related Airy distributions, linewidths, finesse, and performance at low or frequency-dependent reflectivity." In: *Optics Express* 24.15 (July 25, 2016), p. 16366. ISSN: 1094-4087. DOI: 10.1364/OE.24.016366. URL: <https://www.osapublishing.org/abstract.cfm?URI=oe-24-15-16366> (visited on 05/13/2019) (cit. on pp. 17, 18).
- [14] *Fabry-Pérot interferometer - Wikipedia*. URL: https://en.wikipedia.org/wiki/Fabry%20%93P%C3%A9rot_interferometer (visited on 05/06/2019) (cit. on pp. 19, 21).
- [15] Amnon Yariv, Pochi Yeh, and Amnon Yariv. *Photonics: optical electronics in modern communications*. 6th ed. The Oxford series in electrical and computer engineering. OCLC: ocm58648003. New York: Oxford University Press, 2007. 836 pp. ISBN: 978-0-19-517946-0 (cit. on p. 22).
- [16] Michael Hercher. "The Spherical Mirror Fabry-Perot Interferometer." In: *Applied Optics* 7.5 (May 1, 1968), p. 951. ISSN: 0003-6935, 1539-4522. DOI: 10.1364/AO.7.000951. URL: <https://www.osapublishing.org/abstract.cfm?URI=ao-7-5-951> (visited on 05/09/2019) (cit. on p. 25).